Aerodynamic and Aeroacoustic Study of Low Reynolds Number Rotors: Influence of Pitch Angle, Airfoil Camber and Thickness

Pietro Li Volsi, Gianluigi Brogna, David Gomez-Ariza, Romain Gojon, Thierry Jardin, Hélène Parisot-Dupuis, Jean-Marc Moschetta

Aeroacoustics Conferences
June 14-17, 2022, Southampton, UK
28th AIAA/CEAS Aeroacoustics 2022 Conference
10.2514/6.2022-3109

Aerodynamic and Aeroacoustic Study of Low Reynolds Number Rotors: Influence of Pitch Angle, Airfoil Camber and Thickness

Pietro Li Volsi*, and Gianluigi Brogna†
PARROT Drones SAS, Paris, 75010, France

David Gomez-Ariza‡
SENSEFLY, Cheseaux-sur-Lausanne, 1033, Switzerland

Romain Gojon§, Thierry Jardin¶, Hélène Parisot-Dupuis‖ and Jean-Marc Moschetta**
ISAE-SUPAERO, Université de Toulouse, Toulouse, 31400, France

With the increase in the use of micro air vehicles (MAVs), the issue of noise pollution is becoming critical in both military and civilian fields. The main noise component in quadcopter MAVs is generated by the rotors and their interactions with the whole body. Here, a Non-Linear Vortex Lattice/Particle Method (NVLM), coupled with the Farassat formulation-1A of the Ffowcs-Williams and Hawkings (FW-H) acoustic analogy, is used to characterize the influence of the blade pitch and the airfoil shape on the tonal noise and the aerodynamic performance of low Reynolds number rotors typical of MAVs. The validation of both NVLM and FW-H codes is adressed with test cases from the literature and experiments on a 25cm diameter NACA0012 constant-pitch rotor in hovering conditions. The tonal noise of this MAV rotor is then studied in details. Finally, a parametric study of rotor pitch angle and of airfoil camber and thickness is performed, providing guidelines for the design of small rotors with low acoustic footprint and optimal aerodynamic performance.

I. Nomenclature

c	=	chord [m]
c	=	speed of sound [m/s] (in Eq. 6-7)
C_D	=	drag coefficient [-]
C_L	=	lift coefficient [-]
C_L/C_D	=	lift-to-drag ratio [-]
C_Q	=	torque coefficient [-]
C_t	=	thrust coefficient [-]
Δ	=	Laplace operator
dS	=	surface element [m^2]
f	=	frequency [Hz]
f^+	=	dimensionless frequency, $f^+ = f/f_{BPF}$ [-]
FM	=	figure-of-merit [-]
Γ	=	vortex strength [m^3/s]
l_r	=	projection of the loading vector (**l**) onto the observer vector (**r**) [Pa]
$\dot{l}_r$	=	projection of the derivative of the loading vector (**l**) onto the observer vector (**r**) [Pa/s]
l_M	=	projection of the loading vector (**l**) onto the Mach vector (**M**) [Pa]
M	=	Mach number [-] (**M** = the Mach vector)

*PhD Candidate at ISAE-SUPAERO and Aeroacoustic Engineer at PARROT Drones SAS, pietro.livolsi@parrot.com
†Mechanical Simulation and Vibro-Acoustic Technical Leader, PARROT Drones SAS, gianluigi.brogna@parrot.com
‡Aerodynamic and Aeroacoustic Tech Lead, SENSEFLY, david.gomez-ariza@sensefly.com
§Research Associate, Département Aérodynamique, Énergétique et Propulsion (DAEP), AIAA member, romain.gojon@isae-supaero.fr
¶Research Associate, Département Aérodynamique, Énergétique et Propulsion (DAEP), thierry.jardin@isae.fr
‖Associate Professor, Département Aérodynamique, Énergétique et Propulsion (DAEP), helene.parisot-dupuis@isae-supaero.fr
**Professor, Département Aérodynamique, Énergétique et Propulsion (DAEP), AIAA senior member, jean-marc.moschetta@isae-supaero.fr

$\mathbf{n}$	=	surface normal vector
∇	=	gradient function
ν	=	kinematic viscosity $[m^2/s]$
ω	=	vorticity $[1/s]$
Ω	=	rotational speed $[RPM]$
P	=	aerodynamic power [W]
p'	=	total acoustic pressure [Pa]
p'_L	=	loading noise acoustic pressure [Pa]
p'_T	=	thickness noise acoustic pressure [Pa]
PL	=	power loading $[N/W]$
Q	=	torque [Nm]
$\mathbf{r}$	=	observer vector [m]
$\mathbf{r}$	=	radial position of the panel [m] (in Eq. 2)
R	=	rotor radius [m]
$R_{\text{cut-off}}$	=	cut-off radius / rotor radius [-]
Re_c	=	chord-based Reynolds number, $Re_c = (\Omega R c)/\nu$ [-]
ρ	=	density $[kg/m^3]$
T	=	thrust force [N]
θ	=	directivity angle [°]
θ_{pitch}	=	pitch angle [°]
θ_{twist}	=	twist angle [°]
$\mathbf{v}$	=	lattice velocity $[m/s]$
$\mathbf{V}_\infty$	=	freestream velocity $[m/s]$
$\mathbf{x}$	=	lattice position $[m]$
$\mathbf{y}$	=	observer (microphone) position $[m]$

II. Introduction

During the last decade, the micro air vehicle (MAV) market has experienced a significant growth. Nowadays, MAVs are commonly used in both civil and military sectors. In the former they are a very good asset, for example in the cinema and photographic industry (see Fig.1). In the military sector, their use is mostly for reconnaissance purposes. In any case, MAVs are increasingly used because of their low cost, low set-up time and the possibility to fly them in closed and difficult environments. For these reasons, they are intended to replace helicopters in many more applications.

Fig. 1 On the left: The PARROT ANAFI Ai (800 grams) mostly used in the civilian sector. On the right: The PARROT ANAFI USA (500 grams), used in the military field, but also in the industry. [Courtesy of PARROT Drones]

The quadcopter configuration of MAVs brings many advantages, but also has its own drawbacks. In fact, the rotor and body compactness leads to new aerodynamic and aeroacoustic challenges related to:

- the low Reynolds number flow that the rotors face;
- the highly coupled aerodynamic and aeroacoustic interactions between the rotors [1, 2], and the rotors and the body [3];
- the high sensitivity to wind gusts [4].

In the last few years, the research community has been focusing notably on the understanding of low Reynolds number effects on the aerodynamic performance of MAV rotors. The rotors compactness induces a chord-based Reynolds number ranging from $Re_c = 10^4$ to 10^5. In this flow regime, the blades suffer from increased viscous drag, hence reduced aerodynamic efficiency, and can experience separation due to increased viscous forces with respect to inertial forces in the boundary layer. In addition, MAVs rely on batteries with low energy storage. Thus, the aeroacoustic optimization towards acoustically stealthier MAV rotors, which operate at high rotational speeds, should be tightly coupled with aerodynamic optimization [5–12].

The objective of this paper is to analyze the effects of the airfoil camber and thickness and of the blade pitch angle on the aerodynamic and aeroacoustic footprints of a 25cm diameter rotor using a non-linear vortex lattice/particle method (NVLM) coupled with Ffowcs-Williams and Hawkings (FW-H) acoustic analogy. Before comparing different rotors, the NVLM code and FW-H coupling are validated upon data from the literature and experimental data obtained in the ISAE-SUPAERO anechoic chamber on a NACA0012 constant pitch rotor. The tonal noise emitted by this rotor is studied.

Since the actual acoustic code only computes the tonal component of the acoustic spectrum, the validation is done by comparing the 1st and the 2nd blade passing frequency (BPF) sound pressure level (SPL) at different microphone locations (shown in Fig.2). The tests were performed in the ISAE-SUPAERO anechoic room using a directivity antenna of 13 microphones (see Fig.2). Details about the experimental test campaign and the corresponding open database are presented in [13, 14].

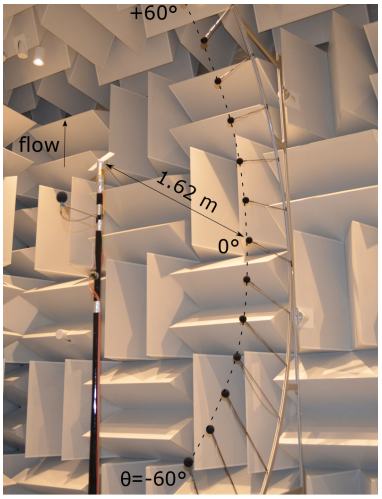

Fig. 2 ISAE-SUPAERO anechoic chamber and microphone locations ranging from $\theta = -60°$ to $\theta = 60°$ at a constant distance of 1.62m away from the rotor center. Positive microphone angles indicate the induced flow direction.

After the presentation of the numerical method in Sec.III.A and III.B, the aerodynamic solver and the acoustic code are first validated in Sec. III.C, and then they are used to study the aeroacoustics of different rotor configurations in Sec.IV. The main conclusions are summarized in Sec.V.

III. Methodology

A. Aerodynamic simulations

1. Vortex Lattice Method

The vortex lattice method (VLM) relies on potential flow theory, with the following assumptions:

- the flow is:
  - incompressible $\rightarrow \nabla \cdot \mathbf{V} = 0$;
  - inviscid $\rightarrow \nu = 0$;
  - irrotational $\rightarrow \nabla \wedge \mathbf{V} = \mathbf{0}$;

- the lifting surfaces are considered thin (with respect to the chord).

These assumptions lead to a conservative vector field, that is, the velocity vector is equal to the gradient of a potential flow:

$$\mathbf{V} = \nabla(\phi) \tag{1}$$

which satisfies **Laplace's equation** ($\Delta(\phi) = 0$). Since Laplace's operator Δ is linear, different potential flows can be linearly added to create more complicated flows. These elementary potential flows can be freestream velocities, point sources and sinks, doublets and vortex filaments/panels. In the case of the VLM, the final flow field is a combination of elementary **vortex rings** (or panels with constant strength Γ). Since the rotor blade is discretized into $N_i \times N_j$ lattices, N_i and N_j being the number of lattices along the chord and span, respectively, the circulations of the vortex rings to be calculated are noted $\Gamma_{i,j}$[15]. The application of the Kutta condition, alongside with the non-penetration condition at the blade surface (Eq.2) allows for the calculation of the circulations $\Gamma_{i,j}$.

$$\mathbf{V}_{inflow} \cdot \mathbf{n} = (\mathbf{V}_{induced(blade)} + \mathbf{V}_{induced(wake)} + \mathbf{V}_{\infty} - \mathbf{\Omega} \times \mathbf{r}) \cdot \mathbf{n} = 0 \tag{2}$$

where $\mathbf{n}$ is the normal to the surface of the panel, $\mathbf{\Omega}$ is the rotor rotational speed, $\mathbf{r}$ is the radial position of the panel and $\mathbf{V}_{\infty}$ is the flight speed.

Once the influence matrix is created and both circulation and the inflow velocity $\mathbf{V}_{inflow}$ computed, the effective angle-of-attack ($\alpha_{eff,j}$) of each spanwise section is calculated through the following formula:

$$\alpha_{eff,j} = \theta_{pitch,j} + \theta_{twist,j} + \alpha_{induced,j} \tag{3}$$

Non-linearity is then introduced, as detailed in subsection III.A.2.

2. Non-Linear VLM

As described in subsection (III.A.1), the vortex lattice method derives from the potential flow theory and is, by definition, a linear method. Its application to wings and rotors under low Reynolds number conditions, where viscous effects may induce non-linear phenomena and strongly impact aerodynamic and aeroacoustic performance, is hence not fully appropriate. For this reason, Jo et al. [16] developed a VLM code that takes into account part of the low-Reynolds-number-induced non-linearities through look-up tables (Fig.3).

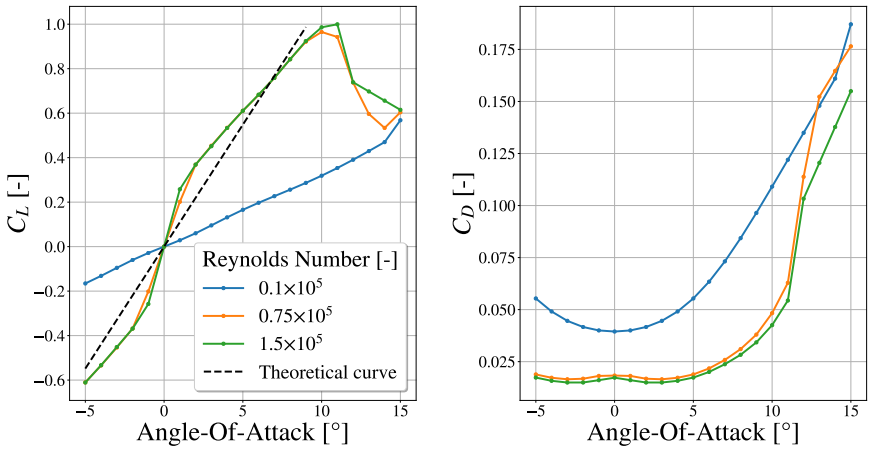

Fig. 3 Look-up table of the NACA0012 profile computed via XFOIL[17] (with N_{crit} = 8 [18]). c_L coefficients (on the left) and c_D coefficients (on the right), as functions of the Angle-of-Attack for three different Reynolds numbers.

The look-up table procedure is divided into five steps:

1) the sectional bound circulation strength is calculated from the linear VLM, as well as the contribution of each chordwise lattice (chordwise circulation ratio);
2) induced velocity $\mathbf{V}_{induced}$ is computed at a reference point at each section;
3) the lift coefficient corresponding to the $\mathbf{V}_{induced}$ and α_{eff} for each section are calculated through the look-up table;
4) the circulation value for each surface lattice is updated according to the lift coefficient;
5) if the convergence criterion is not satisfied, another iteration is necessary.

When the non-linear loop ends, the chordwise circulation strengths are calculated by taking the initial chordwise circulation ratii as reference and scaling them with the new sectional bound circulation strength. Once the non-linear correction is achieved, the forces are calculated and wake vortices are shed (see subsection III.A.3), a new time step is started.

3. Vortex Particle Method

One of the main advantages of NVLM codes is the implementation of meshless calculations to simulate the wake. As explained in [16], [19] and [1], the code models the wake through a vortex particle method (VPM). This method consists in shedding vortex particles (or blobs, each with a circulation strength and a core radius) from the blade trailing edge into the wake. For convergence and stability purposes, a free wake model is also implemented and the vortex particles are shed after the third row of the free-wake lattices (red wake lattices of Fig.4). These particles are convected into the wake and they influence each other. That is, the VPM computational time depends on the number of particles N_p in the order of $O(N_p^2)$. To increase the efficiency of the code, Jo et al. [19] implemented a Fast Multipole Method which reduces the computational time cost to $O(N_p \log N_p)$.

The vorticity field induced by the wake (composed of N_p particles) at a location $\mathbf{x}$ in the flowfield is calculated as follows:

$$\omega(\mathbf{x}, t) = \nabla \times \mathbf{V} = \sum_{i=1}^{N_p} \mathbf{\Gamma}_i(t) \zeta_{\sigma_i}(\mathbf{x} - \mathbf{x}_i(t)) \tag{4}$$

With:

- $\mathbf{x}$ the location in the flowfield and $\mathbf{x_i}$ the location of the i^{th} particle;
- t the physical time;
- $\zeta = \zeta(\mathbf{x}/\sigma)/\sigma^3$ is the regularized vorticity distribution function within the core of the particle (σ is the core size).

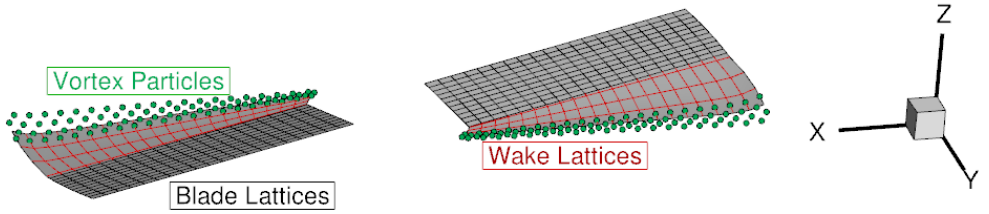

Fig. 4 Simulation snapshot showing the blade lattices (in black), the wake lattices (in red) and the vortex particles (in green).

B. Far-field acoustic calculations

The experimental frequency spectrum [13, 14] of a rotor noise measured at a far-field observer position of Fig.5 shows discrete peaks at different frequencies (referred to as tonal noise) and a broadband noise [20][21]. The non-highlighted tonal peaks at the rotational speed (RPM) frequency and its odd harmonics are probably due to the non perfectly balanced rotor blades and will not be examined in this paper. The broadband noise is composed of different unsteady phenomena involving turbulence: the blade wake interaction (BWI), the trailing edge noise, the boundary layer separation noise and the vortex shedding noise. In real conditions (external to the anechoic chamber controlled environment), the turbulence ingestion noise is a very important part of the broadband noise. In this paper, the attention is focused on the tonal noise. The rotors tonal noise is generated by different sources:

- the thickness noise produced by the displacement of the fluid due to the passage of the rotor blades;
- the loading noise characterized by the (steady and unsteady) pressure distribution along the chord and the span of the blades;
- the blade vortex interaction (BVI) produced by the impact of the blade tip vortex on the next blade;
- the high-speed impulsive noise present when the tip of the blade is transonic.

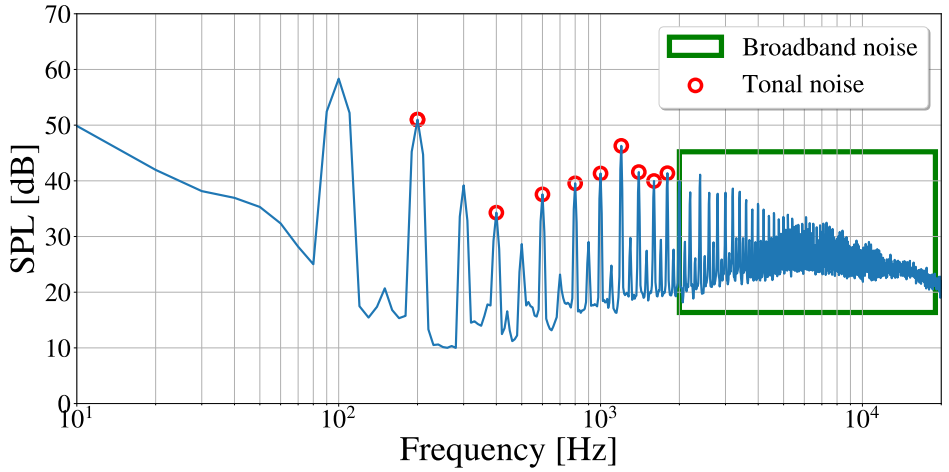

Fig. 5 Experimental SPL spectrum of a NACA0012 rotor at 6000RPM taken from a microphone located 1.62m away from the rotor center at 60° angle [13, 14]. The tonal peaks are highlighted by the red circles, while the high-frequency broadband noise is emphasized by the green rectangle.

To capture the far-field aeroacoustic noise emitted by the rotors and their directivity, the Farassat formulation-1A [22] of the FW-H acoustic analogy has been implemented. This formulation consists in calculating the near- and far-field noise generated by three different sources: the monopole, the dipole and the quadrupole. Because of the nature of the NVLM code used for this study, the tonal noise calculated is composed of monopole sources, previously called thickness noise, and dipole sources, or loading noise (the quadrupole noise is not calculated).Since lattices do not radiate to the observer at the same time, the 'retarded time' (τ) must be calculated and the acoustic pressure evaluated at this retarded-instant. The acoustic pressures of each lattice are added to calculate the whole rotor acoustic pressure. The rotor total tonal noise is therefore the contribution of both loading and thickness noise:

$$p'(\mathbf{x},t) = p'_T(\mathbf{x},t) + p'_L(\mathbf{x},t) \tag{5}$$

- The thickness noise is affected by the blade geometry (through the **n** normal vector) and the rotational speed (through the velocity (v) and Mach (M) vectors);

$$4\pi p'_T(\mathbf{x},t) = \int_{f=0} \left[\frac{\rho_0(\dot{v}_n + v_{\dot{n}})}{r\,(1-M_r)^2} \right]_{ret} dS + \int_{f=0} \left[\frac{\rho_0 v_n (r\dot{M}_r + cM_r - cM^2)}{r^2\,(1-M_r)^3} \right]_{ret} dS \tag{6}$$

- The loading noise depends on both steady and unsteady pressure distribution on the blade through the terms l and its derivative $\dot{l}$;

$$4\pi p'_L(\mathbf{x},t) = \frac{1}{c}\int_{f=0} \left[\frac{\dot{l}_r}{r\,(1-M_r)^2} \right]_{ret} dS + \int_{f=0} \left[\frac{l_r - l_M}{r^2\,(1-M_r)^2} \right]_{ret} dS + \frac{1}{c}\int_{f=0} \left[\frac{l_r(r\dot{M}_r + c(M_r - M^2))}{r^2\,(1-M_r)^3} \right]_{ret} dS \tag{7}$$

$$\tau = t - \frac{r}{c} = t - \frac{|\mathbf{x}-\mathbf{y}|}{c} \tag{8}$$

With:

$$l_r = l_i \hat{r}_i \quad \dot{l}_r = \dot{l}_i \hat{r}_i \quad l_M = l_i \hat{M}_i$$

In the following subsection, the aerodynamic and tonal noise calculations are assessed upon analytical solutions and real rotor tests taken from the literature.

C. Validation

1. Aerodynamic validation

The aerodynamic computational performance of the NVLM code was first validated [19] upon experimental data obtained on a commercial rotor by Zawodny and Boyd [3]. Here, further comparison with homemade rotors is provided. The two-bladed NACA0012 rotor illustrated in Fig.6 is used and operated at a rotational speed of 6000RPM. The corresponding rotor and simulation parameters are summarized in table 1.

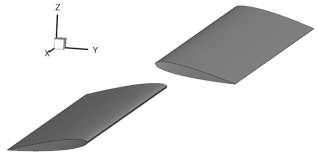

Fig. 6 The rotor used in the simulation for the correlation with the experimental data.

Rotor parameters	
# of blades	2
Airfoil Section	NACA0012
Chord Length [m]	0.025
Diameter [m]	0.25
Pitch angle (θ_{pitch}) [°]	10
Twist angle (θ_{twist}) [°]	0
Root cut-off ($R_{\text{cut-off}}$)	15% of the Radius
Blade discretization	
# of Chordwise Lattices	11
# of Spanwise Lattices	20
# of Wake Lattices	3
Simulation parameters	
Revolutions simulated [-]	30
Rotational speed [RPM]	6000
Step angle [°]	5
Timestep [s]	~0.00014
Average interval [revs]	20 - 30

Table 1 Simulation parameters used for the validation of the NVLM code.

The thrust and torque obtained by NVLM computations for this configuration are $2.88N$ and $4.72 \cdot 10^{-2} N.m$, which differ by 1.9% and 1.5% from the values reported by Jo et al. [19] using a similar approach, respectively.

Results are further compared with experimental data obtained in ISAE-SUPAERO anechoic chamber, reported by Gojon et al. [13] and available on [14], in terms of thrust and torque coefficients $c_T = T/(\rho f^2 D^4)$ and $c_Q = Q/(\rho f^2 D^5)$, respectively. The results in Table 2 show differences of 7.1% and 8.1% in thrust and torque coefficients, respectively. These differences are reasonable given the fact that different experiments on different specimen of a given rotor geometry can lead to discrepancies on the order of 10%, as previously highlighted by Deters et al. [23] on commercial rotors. Similar differences were here found using homemade rotors with different manufacturing methods and materials and different test benches where interactions between rotor wake and mountings can be different.

	Experimental data (Gojon et al. [13])	NVLM simulation
Thrust coefficient c_T [-]	0.0649	0.0603 (-7.1%)
Torque coefficient c_Q [-]	0.00429	0.00394 (-8.1%)

Table 2 Thrust and torque coefficients comparisons.

2. Acoustic validation

Before comparing the tonal noise code based on Farassat formulation-1A to real rotor cases, two test-cases allowed to separately validate both loading and thickness noise components.

As explained in section III.B, the loading noise depends on the loading distribution on the surface of the blade, its rotational speed and the microphone location. Two different test-cases (and different parameters) from Casalino [24] were used to validate the loading noise component of the tonal noise. These test-cases are based on radial and axial dipoles rotating and translating with respect to a fixed observer. As shown in both figures 7 and 8, for rotating and non-translating dipoles, the present FW-H simulation results are superposed to the analytical solution (see [25, pp. 269–275]) used by Casalino to validate his advanced time approach model . When the dipoles translate at high velocity ($\sim$ 70m/s and $\sim$ 140m/s), small differences between the coded FW-H and the analytical solutions arise in the transition part. The capabilities of the present Farassat formulation-1A is validated for this study, that takes into account only free rotors in hovering flight conditions.

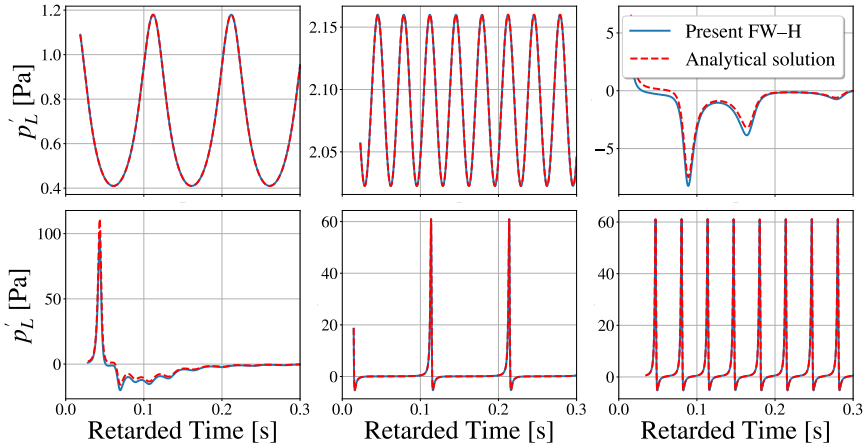

Fig. 7 Comparison between Casalino test cases B and the FW-H acoustic simulations.

The thickness noise validation test is based on the Brentner test-case. This one has been used by Hirsch et al. [26], Ghorbaniasl and Hirsch [27] and it is based on the thickness noise prediction of a conventional helicopter rotor obtained by Brentner [28]. The helicopter rotor parameters are summed-up in table 3 and the comparisons in both temporal and frequency domains are shown in Fig.9.

The tonal noise predicted by the NVLM code and the Farassat formulation-1A has been validated by comparing it with experiments performed previously at ISAE-SUPAERO [13, 29] in the frequency domain. For comparison purposes, both experimental and numerical data are processed as follows. The experimental acoustic data are acquired at a sampling frequency of 51.2 kHz, during 16s. The acoustic narrow band spectra are obtained from time signals by dividing the main 16s signal into 0.10s duration signals with 50% overlap. The Hanning window is then applied, the fast Fourier transform (FFT) is computed and the amplitude correction factor is applied.

Finally, the SPL is obtained through the following formula:

$$SPL(f) = 10\log_{10}\left(\frac{p'^2_{rms}(f)}{P_0^2}\right) \tag{9}$$

with $P_0 = 2\times10^{-5}Pa$ and p'_{rms} is the root mean squared (RMS) acoustic pressure.

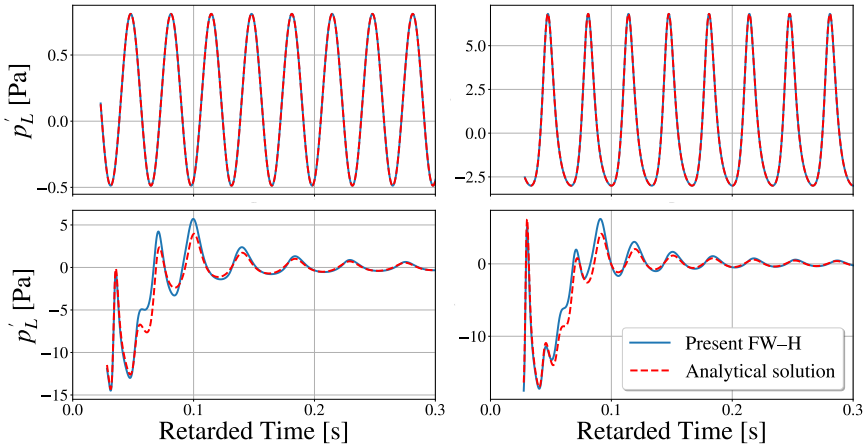

Fig. 8 Comparison between Casalino test cases C and the FW-H acoustic simulations.

Brentner rotor parameters	
Rotor	1/4th scale UH-1 rotor
# of blades	2
Airfoil Section	NACA0012
Chord Length [m]	0.1334
Radius [m]	1.829
Pitch [°]	15.0
Twist [°/m]	-10.9
Root AoA (θ_{root}) [°]	14.07
Tip AoA (θ_{tip}) [°]	4.1
Root cut-off ($R_{\text{cut-off}}$)	8.5% of the Radius
Simulation parameters	
Revolutions simulated [-]	10
Rotational speed [RPM]	1296
Step angle [°]	0.9
Average interval [revs]	0 - 10
Microphone location	
Microphone distance [m]	3.0
Directivity angle [°]	0.0

Table 3 Simulation parameters used for the thickness noise validation.

The simulated frequency noise spectrum for a microphone in the rotor plane (1.62m away from the rotor center) is shown in Fig.10.

Directivity plots of the 1st and 2nd BPFs comparing simulation and experimental results are shown in Fig.11. This plot shows good predictions of the 1st BPF directivity (differences lower than 3dB) for microphones located in the rotor wake half-plane. Above the rotor, however, differences between 3dB and 8dB are observed. The 2nd BPF, instead, shows good agreement in a larger region, with differences lower than 5dB between -30° and +50°. On the other hand, discrepancies exist out of this range, particularly in the experimental directivity pattern below -40° (which may arise from experimental uncertainties).

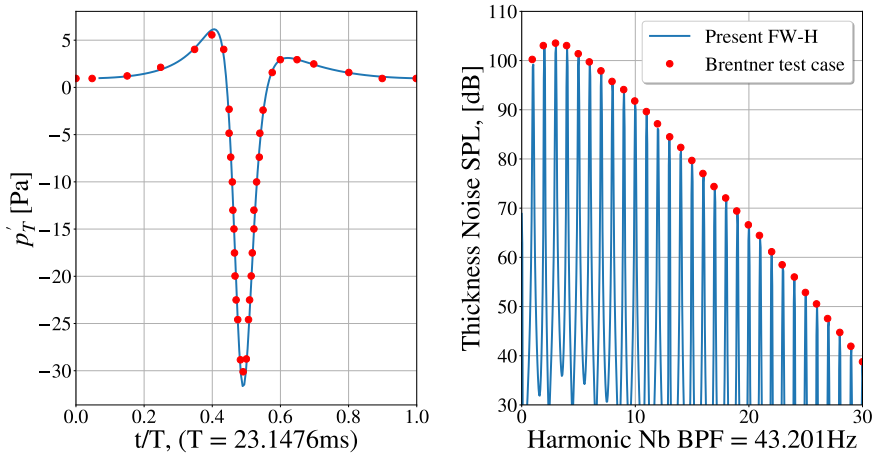

Fig. 9 Comparison between Brentner test-case and present FW-H Farassat formulation-1A of the thickness noise.

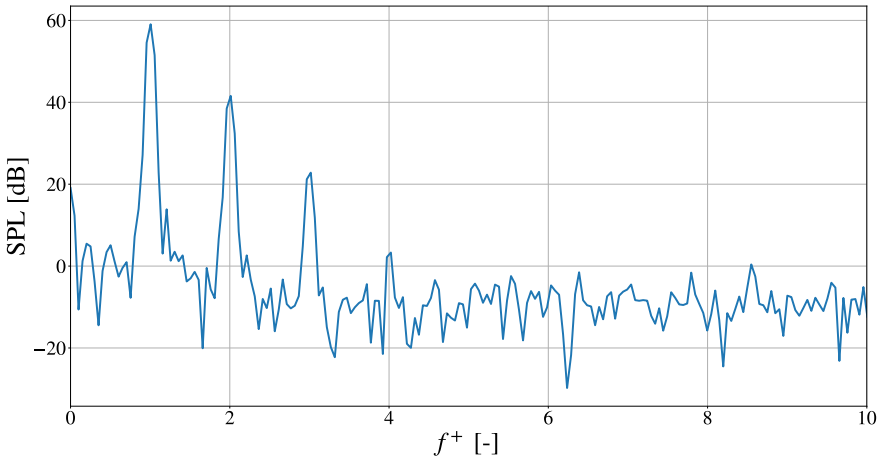

Fig. 10 Sound pressure level as function of the blade passing frequency harmonics.

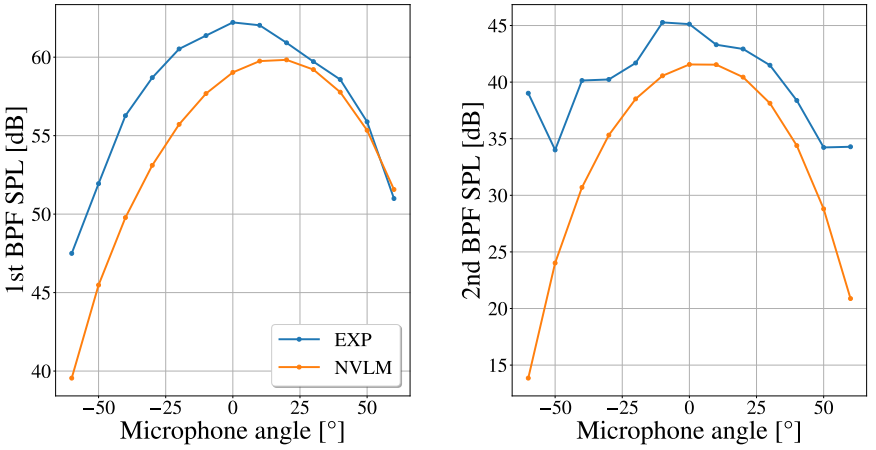

Fig. 11 Directivity of the amplitude of the 1stBPF (graph on the left) and 2ndBPF (graph on the right). Comparisons between experimental results [13] and NVLM predictions.

3. Influence of NVLM parameters

In this subsection, we report on the influence of NVLM parameters on computational cost and aerodynamic and aeroacoustic performance. The aim here is to define relevant computational parameters to obtain accurate results with reduced computational costs. In that sense, we focus on three main parameters: the spatial resolution, number of rotations simulated and particle deletion.

Table 4 shows results obtained with and without vortex particle deletion and for 15 and 30 simulated rotations. Particle deletion is applied at a radial distance of 0.3m away from the rotor center (2.4 times the rotor radius), which is assumed from previous experiments on ground effect to have little impact on rotor performance [30]. Time-averaging of thrust and torque signals is achieved during one-third of the total simulated time.

Configurations	Sim Time [hCPU]	Thrust [N]	Torque [Nm]
20-30 AV revs - w/o Del (REF)	2054	2.88	0.0472
20-30 AV revs - w Del	576 (-71%)	2.91 (+1.0%)	0.0476 (+0.8%)
10-15 AV revs - w/o Del	418 (-80%)	2.89 (+0.3%)	0.0476 (+0.8%)
10-15 AV revs - w Del	264 (-87%)	2.93 (+1.7%)	0.0479 (+1.5%)

Table 4 Aerodynamic trust and torque and computational cost comparison between different configurations: AV revs = Average intervals in revolutions; wo Del = Without vortex particle deletion; w Del = With vortex particle deletion.

Differences in aerodynamic performance obtained from different parameter settings are found to be negligible while the computational time can be reduced up to 87% by applying particle deletion and reduced number of rotations. A directivity study, not shown here for the sake of conciseness, also demonstrated a negligible impact on acoustic signals.

Similarly, the influence of blade spatial discretization is shown in Table 5. Here again, the reduction in the number of both chordwise and spanwise lattices down to 5×10 has a negligible impact on the prediction of aerodynamic performance but significantly reduces computational costs.

Finally, Table 6 shows the SPL at the first and second BPF obtained for the reference simulation used in the previous comparison with experiments and the simulation with reduced spatial discretization, reduced number of rotations and particle deletion. Again, it is found that these changes in NVLM parameters have a negligible impact on the acoustics, at least regarding principal tonal components. For this reason, in order to make expensive parametric simulations "10-15 AV revs - w Del" have been chosen. This allowed to run more calculations without decreasing their precision.

IV. Results

As initially introduced, the main objective of this paper is to evaluate and analyze the influence of the blade pitch angle θ_{pitch} and the blade sectional (airfoil) shape on rotor tonal noise, in addition to their aerodynamic performance. First, the NACA0012 constant pitch rotor tonal noise is studied in IV.A. Then a detailed analysis of the NACA0012 10° pitched rotor is conducted, and, is followed by the parametric studies of the airfoil thickness and camber. In order to test different rotor geometries, the simulation parameters used are those reported in subsection III.C.3 that minimize computational cost. As the 4-digits NACA series [31] airfoils allow the modification of both the airfoil thickness and camber independently, they have been chosen to analyze the influence of the airfoil shape.

Discretization Configurations		Sim Time [hCPU]	Thrust [N]	Torque [Nm]
Chordwise	Spanwise			
11	20	264	2.93	0.0479
5	10	93 (-65%)	2.99 (+2.0%)	0.0485 (+1.2%)

Table 5 Aerodynamic main results and computational cost comparison between different configurations.

Configurations	1st BPF SPL [dB]	2nd BPF SPL [dB]
1120 - [20-30 AV revs] - [w/o Del] (REF)	58.98	41.42
0510 - [10-15 AV revs] - [w Del]	59.12 (+0.14dB)	41.24 (-0.18dB)

Table 6 Tonal noise comparison for different simulation configurations for a microphone angle of 0° and distance of 1.62m away from the rotor center.

A. Acoustic decomposition of the rotor noise

The simulated 1st BPF SPL directivity plot of Fig.11 shows a maximum located at a microphone angle of 10°. To better understand this directivity shape, the total acoustic pressure is decomposed into three components: the thickness noise, the steady loading noise and the unsteady loading one. To calculate these two last components, the lattice loading has been split into two components: an averaged (called "steady") and a fluctuating ("unsteady") one, and the noise emitted by both is propagated:

$$\left|l_i(t)\right| = \underbrace{\overline{|l_i|}}_{\text{average}} + \underbrace{\left|l_i(t)\right|'}_{\text{fluctuation}} \tag{10}$$

With:

$$\overline{|l_i|} = \frac{1}{N_{timesteps}} \sum_{t=t_{start}}^{t_{end}} \left|l_i(t)\right| \tag{11}$$

$$t_{start} = \text{20th rotation}$$

$$t_{end} = \text{30th rotation}$$

Once the different acoustic pressures are extracted, the SPL is computed by applying the same post-processing used for the total signal. The directivity of these three new signals is plotted alongside the total signal in the left graph of Fig.12.

Here it is observed that the thickness noise has a maximum in the rotor plane and is the predominant component for a microphone angle range going from $-80°$ up to 10°, where the steady loading noise matches the thickness noise level and becomes even higher at higher microphone angles. The unsteady loading noise has a minimum level in the rotor plane and maxima at -90° and +90°, showing a typical dipole directivity shape.

However, the total noise is lower than the thickness noise between $-80°$ and $-20°$ and always higher than both unsteady and steady loading noise signals. To understand this phenomenon, on the right graph of Fig.12, the phase has been plotted. Here, different phase directivities are observed. While the thickness noise phase is almost constant for all the microphone angles going from -80° to +80°, the steady loading noise shows a gradual decrease in the phase going from -90° to +80°. This gradual reduction of the steady loading noise phase, coupled with the constant and opposite thickness noise phase, explains why from -80° to -20° the total noise is lower than the thickness noise. In this range, in fact, a destructive interference between the steady loading and thickness noise components occurs. In the region [-10°; +80°], due to the change in phase of the steady loading noise, the interference evolves into a constructive one and the total signal becomes higher than both components.

The steady loading noise SPL and phase directivities are different from the usual dipole and monopole general shapes. Since the understanding of the steady loading directivity is not straightforward, its simplification can lead to a better comprehension of the phenomena involved.

The acoustic pressure of the steady loading component takes into account the force vectors applied at each lattice composing the blades. The NACA0012 rotor reference simulation, has an amount of 440 blade lattices (11 chordwise lattices × 20 spanwise lattices × 2 blades).

Since the rotor external radius is very small compared to the microphones' distance (0.125m vs 1.62m), the blades can be considered as two compact sources rotating around the rotor axis. Both rotor thrust and torque have been applied at 0.1m, i.e. 80% of the rotor external radius. This value has been arbitrarily chosen, but it is coherent with the literature, where it is indicated that the blade thrust/torque overall distribution that can degenerate into a point source at around 75%-80% of the blade span (see Leishman [32]).

Fig.13 shows a comparison between the steady loading noise coming from the NVLM blade force distribution and the rotating dipoles ($L_i V_E$ decomposition). Both SPL and phase directivities match very well, which validates the

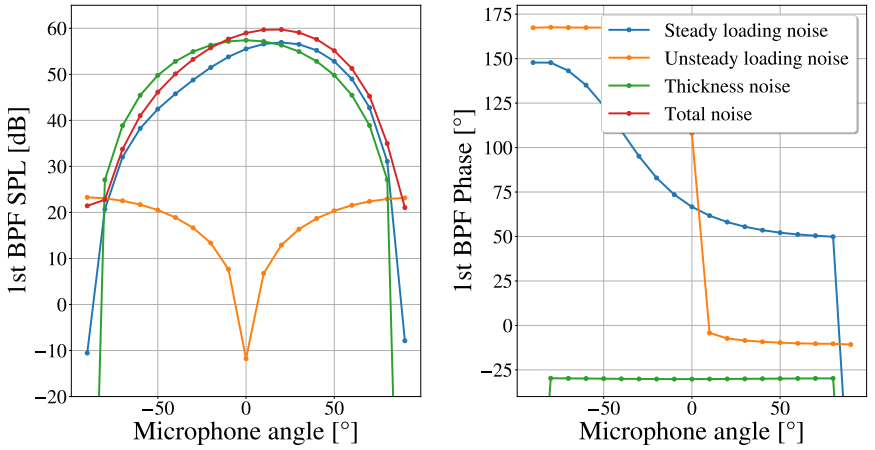

Fig. 12 Directivity of the amplitude of the 1stBPF (graph on the left) and its phase (graph on the right). Influence of the thickness noise and both unsteady and steady loading noise.

compactness hypothesis.

The rotating dipole force vector was further decomposed into two different vectors and their noise propagated:

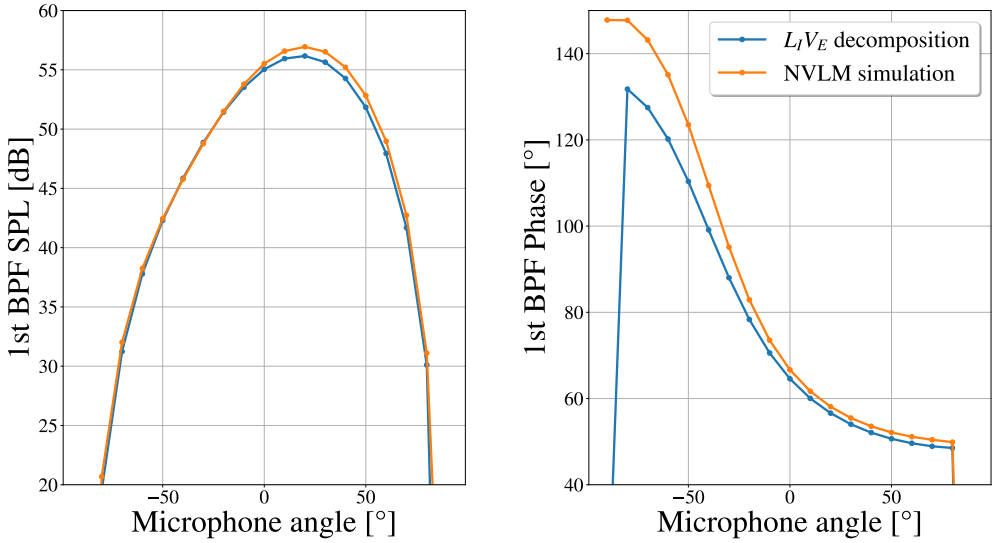

Fig. 13 Directivity of the amplitude of the 1stBPF (graphs on the left) and its phase (graphs on the right) corresponding to the rotor thrust and torque (T = 2.892N, Q = 0.047Nm), 2 blades and Ω = 6000RPM. Comparison with the NVLM simulation

- An axial force vector pointing upward in order to simulate a pure thrust force. The total thrust absolute value corresponds to the full rotor simulated thrust;
- A tangential force vector, in the direction of the dipole velocity vector (but of opposite sign) to simulate a pure torque and whose force value is equal to the full-rotor torque divided by the distance of the dipole from the rotation axis (0.1m).

The new signals, as well as the previous rotating dipoles with the rotor force vector, are plotted in Fig.14. Both pure-thrust and torque signals have a symmetrical directivity shape centered at 0°, while the total steady loading noise directivity is not symmetric. This is, again, due to constructive/destructive interactions between the pure-thrust and torque signals. From -90° to 0°, both pure-force signals have opposite phases, hence the total signal is lower then the two others because of a destructive interference. At 0°, the pure-thrust signal drastically changes phase and its interaction

with the pure-torque noise signal becomes constructive. This explains the maximum located at 20°.

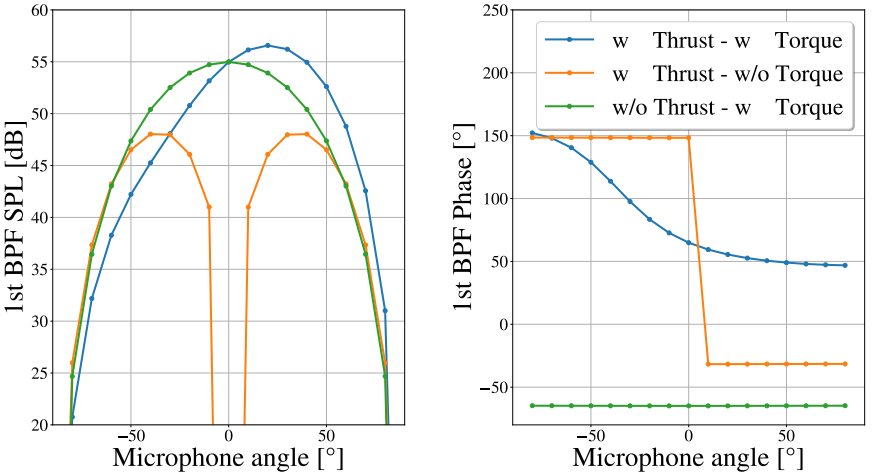

Fig. 14 Directivity of the amplitude of the 1stBPF (Graphs on the left) and its phase (Graphs on the right) corresponding to the two dipoles rotating at Ω = 6000RPM. The blue curve simulates two dipoles with the same thrust and torque as the full rotor. The orange and green curves show a pure thrust and a pure torque, respectively.

In conclusion, for this NACA0012 constant pitch rotor configuration, the 1st BPF total tonal noise is the contribution of different components: the thickness noise and the loading noise. The first one is predominant upstream the rotor and is lower than the steady loading noise downstream. The total noise, due to destructive interferences upstream the rotor, is lower than the thickness noise. However, this rotor is not aerodynamically, nor aeroacoustically optimized and the NACA0012 profile is very thick compared to the ones used in the commercial rotors (E63/Clark Y in APC rotors as an example). For this reason, in the following subsections, the influence of pitch angles, thickness and camber of the airfoil are studied.

B. Influence of the Pitch angle

We first look at the influence of the pitch angle (θ_{pitch}). It is straightforward that an increase in θ_{pitch} induces an increase in effective angle of attack α_{eff} (e.g. Equation 3), hence an increase in rotor thrust, providing that local blade sections do not stall.

Since rotor thrust is dependent on the square of the rotational speed (i.e. $T = c_T \rho \Omega^2 D^4$), a quadratic fit is used to interpolate data at any values of RPMs and study all the rotor configurations at iso-thrust. Note that this is strictly valid for constant c_T values, or linear dependency of c_T with respect to RPM, which depends on Reynolds number effects. Hence care should be taken in the low Reynolds number regime typical of MAV rotors, i.e. where Reynolds number effects may be strong. To reach the target thrust, a calculation at 6000RPM is run, the "a" coefficient of the quadratic law ($T = a \cdot \Omega^2$) is calculated, the rotation speed $\Omega_{\text{target thrust}}$ is deduced and another aerodynamic calculation is run.

The tonal noise is also related to the rotational speed. In this case, it is straightforward that an increase in pitch angle leads to an increase in sectional lift coefficient (again providing that stall does not occur), hence to a higher lattice load l and an increase in the loading noise component (Eq.7). In addition, for a fixed pitch angle, an increase of the rotational speed implies an increase of the blade lattice velocities $\mathbf{v}$ and, consequently, of the thickness noise component (Eq.6).

The design of a quadcopter MAV rotor in hovering conditions generally relies on a thrust constraint, with each rotor thrust equal in magnitude to one fourth of the MAV weight. In what follows, the influence of blade geometrical parameters is analyzed for a given target thrust of 2N, corresponding to a hovering MAV total mass <800 grams.

Given a target thrust, a first parameter to look at and optimize is the power loading $PL = T/P$ (or its dimensionless counterpart, the Figure-of-Merit) which gives an indication on how much power is needed to sustain a given weight. That is, the higher the PL, the lower the power needed to sustain the same amount of weight.

In light of the above considerations, the following Fig.15 shows the rotational speed Ω, the 1st BPF SPL of the total, thickness and loading noise components for a microphone located in the rotor plane, and the Power Loading as a

function of the pitch angle θ_{pitch} at 2N isothrust.

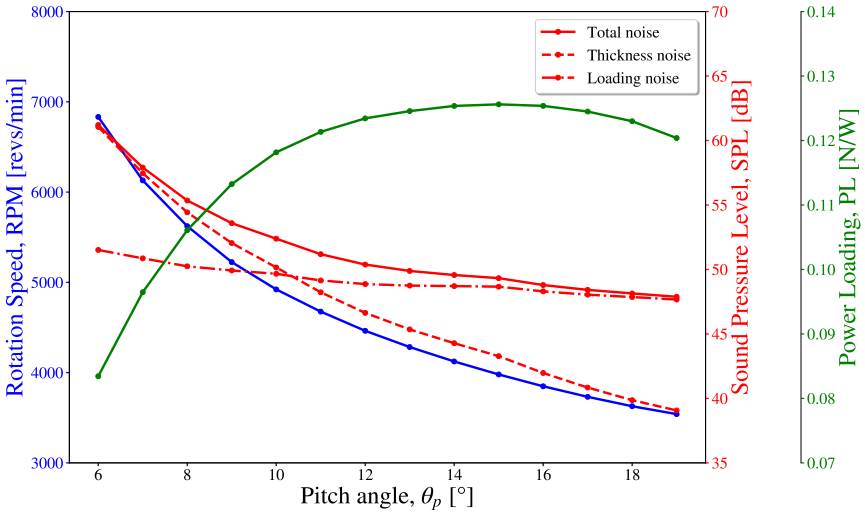

Fig. 15 Rotational speed (blue line), SPL of the 1stBPF (red line) for a microphone located in the rotor plane and power loading (green line) plotted as function of the blade pitch angle at 2N isothrust.

Results from this graph can be summarized as follows:

- The rotational speed required for a 2N thrust decreases when the pitch angle increases. The ratio between the rotational speed of the 6° pitch angle and that at 19° pitch angle is almost two;
- The total noise SPL of the 1st BPF decreases with a similar trend to that of the rotational speed. The ΔSPL of the total noise between the 6° pitch angle and the 18° pitch angle is equal to 15dB;
- The efficiency of the rotor increases between 6° and 14°. Beyond 15°, the power loading monotonically decreases.

The lower rotational speed at a higher pitch angle is due to an increased α_{eff}, hence a higher local lift coefficient of the blade sections. As Fig.15 shows, the thickness noise is highly dependent on the rotational speed of the rotor. This component is higher than the loading noise for pitch angles going from 6° to 10° and the total noise is driven by the thickness noise. After 10° angle, the loading noise becomes preponderant. However, the ΔSPL between the 6°and 19° pitch value is less than 5dB. This suggests that in the loading noise, and for a microphone angle located in the rotor plane, the total thrust of the rotor plays a more important role than the rotational speed. On the other hand, the rotational speed is the key parameter in the generation of thickness noise.

In conclusion, for a constant pitch rotor with a NACA0012 constant section, the pitch angle to choose for aerodynamic purposes is 15°, because the power loading is the highest, hence its endurance is the highest. However, the total noise emitted by this rotor is higher than the least noisy one, the 19° angle, by about 3dB.

C. Influence of the Airfoil Thickness

The interest in the airfoil thickness for low Reynolds numbers has recently grown, due to the introduction of MAVs. Previous works [33, 34] have shown that the thickness plays a prominent role in the aerodynamics of symmetric NACA airfoils at Reynolds numbers in the order of 10^4 - 10^5, with significant influence on the occurrence of laminar separation bubbles (LSBs) and advanced stall for airfoils with large thicknesses. Because of mass and inertia constraints and low Reynolds number encountered, MAV rotors airfoil thicknesses are generally low.

To understand the implications of the airfoil thickness on MAV rotors from both aerodynamic and aeroacoustic points of view, the performance of different airfoil thicknesses are presented, ranging from the NACA 0007 to the NACA 0015 airfoils (the NACA 0012 being the reference one). On NACA airfoils, the maximum thickness is located at ~ 30% of the chord. As done in subsection IV.B, the rotational speed, the power loading and the 1st BPF SPL (of the total noise and loading/thickness noise components) at 0° microphone angle are plotted as function of the maximum thickness in Fig.16, for a given target thrust of 2N and a constant pitch angle of 10° for all rotors.

The following observations are made:

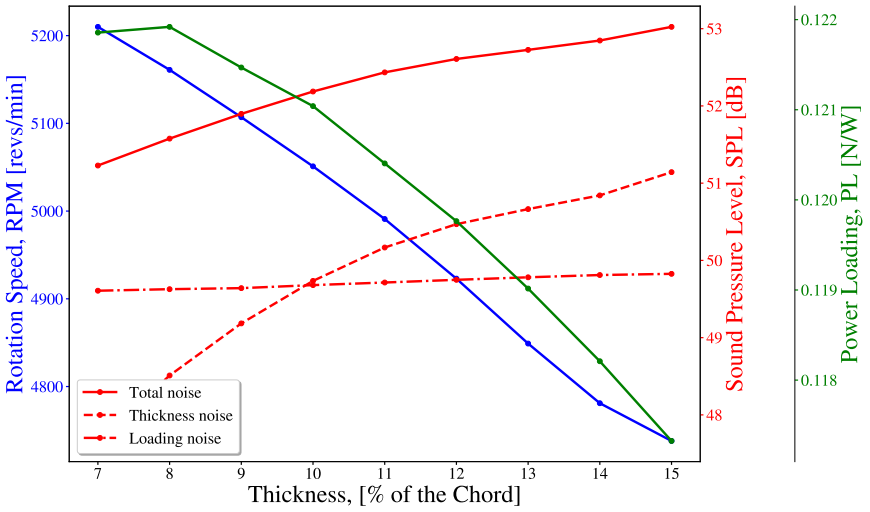

Fig. 16 Rotational speed (blue line), SPL of the 1stBPF (red line) for a microphone located in the rotor plane and power loading (green line) plotted as function of the airfoil thickness for 2N isothrust and $\theta_{pitch} = 10°$.

- The rotational speed steadily decreases ($\sim -400RPM$) due to thicker airfoils generating more thrust when rotating at a certain rotational speed;
- The 1st BPF total SPL increases when the airfoil thickness increases ($\sim +1.8$dB). The thickness noise follows the same trend of the Total SPL, with a higher range (+3dB), while the loading noise does not significantly change for the 0° microphone angle;
- The PL reaches a maximum value for 8% of the airfoil thickness and then it monotonically decreases.

To understand why the aerodynamic performance of the NACA 0008 airfoil are better compared to the others, the lift coefficient, the drag coefficient, as well as the lift-to-drag ratio of the different sections and airfoil thicknesses are displayed in Fig.17. This graph is made by using the look-up tables described in III.A.2. After having run the aerodynamic calculation, both induced sectional Reynolds number and angles-of-attack are averaged and used as inputs of the look-up table, where the sectional C_L and C_D values are calculated.

As mentioned in IV.A, rotor thrust and torque are mainly produced at 75-80% of the blade span. This is verified in Fig.17, where the highest C_L values are produced at 78% and 87% of the blade span (independently of the airfoil thickness). On the other hand, the drag coefficients of the outboard sections are lower than the ones near the root. These considerations explain the higher lift-to-drag ratios for the external sections of the blade.
An increase in the airfoil thickness near the tip sections (where most of the thrust/torque are produced), leads to higher C_L values. This is the main reason why the rotational speed needed to reach 2N of thrust decreases. C_D values at 87% of the span section reaches a minimum for an airfoil thickness of 8% of the chord. Above this maximum thickness value, the C_D value increases. This trend is mirrored in the power loading graph of Fig.16, where the maximum efficiency is reached by the rotor carrying the NACA 0008 airfoil.

From the aeroacoustic point of view, it is remarkable that the increase in the airfoil thickness induces an increase in the thickness noise by 3dB even if the rotational speed decreases. Higher airfoil thickness, in fact, means higher amount of fluid displaced by the rotor blade and, consequently, higher thickness noise component. The loading noise at 0° microphone, however, is not impacted by the airfoil thickness increase. The change in both torque and rotational speed is not high enough to affect the loading noise. It is interesting to note that loading and thickness noise graphs intersect each other for a maximum thickness value of 10%. Below this value, the loading noise is preponderant while, above, the thickness noise becomes higher. This explains why increasing the maximum thickness value from 7% to 15% increases the thickness noise by 3dB, and the total noise by only 1.8dB.
This airfoil thickness parametric study on the 10° pitched MAV rotors at 2N iso-thrust shows that the airfoil thickness is important for the aerodynamic performance of the rotor, but also for the aeroacoustic tonal noise footprint. A 8% thick airfoil, in fact, enhances the aerodynamic performance, but also reduces the thickness noise component of the tonal noise compared to the NACA0012 reference rotor. This thinner airfoil reduces the rotor weight by 33% compared to the NACA 0012. Even if the weight of the rotors is negligible compared to the full drone weight, it is important to limit it in

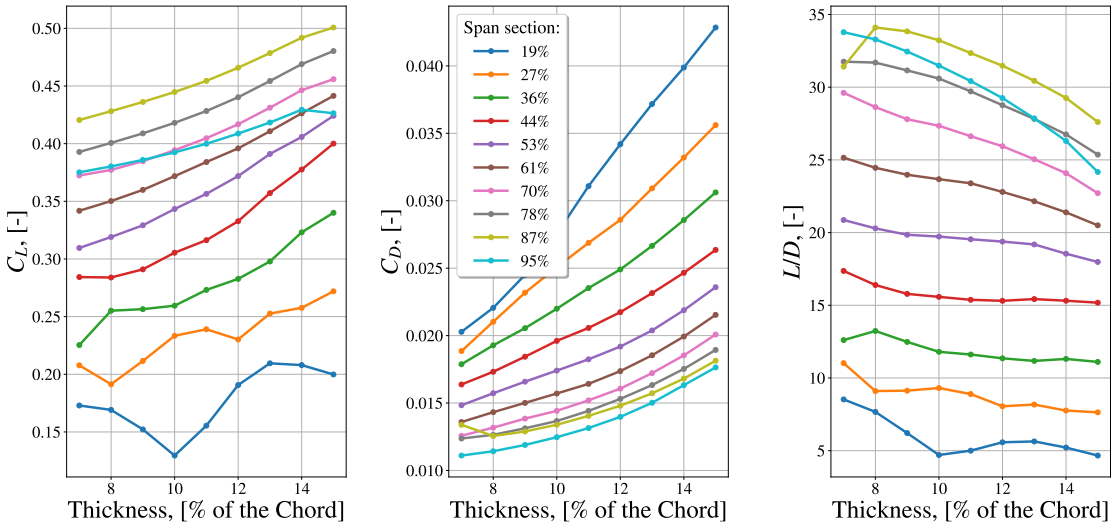

Fig. 17 Sectional lift coefficient, drag coefficient and lift-to-drag ratio as function of the maximum airfoil thickness for different blade spanwise sections.

the design phase. Lower rotor weight due to thinner airfoil (at the same chord distribution) means also lower inertia. This impacts also the mass of the motor since less torque will be required to spin the rotor. The gain of few grams can also allow the addition of other important components useful to better accomplish the missions (cameras, sensors, slightly heavier batteries to increase the flight endurance, etc) or to comply with regulations.

D. Influence of the Airfoil Camber

In this last section, the influence of the airfoil maximum camber onto the aerodynamic and aeroacoustic performance of MAV rotors is investigated. For the sake of conciseness, both thickness and position of the airfoil maximum camber are fixed to 12% and 50% of the chord, respectively. The first digit, corresponding to the maximum camber, is the investigated variable. As for the pitch and thickness parametric study, the rotors are studied at 2N thrust, the pitch angle is fixed to 10° and the microphone is in the rotor plane (at 0° angle).

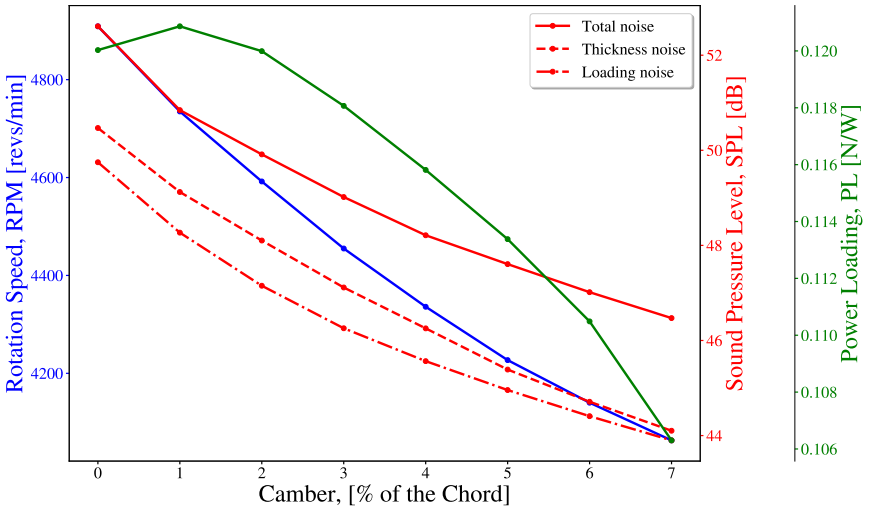

Fig. 18 Rotational speed (blue line), SPL of the 1stBPF (red line) for a microphone located in the rotor plane and power loading (green line) plotted as function of the airfoil maximum camber for 2N isothrust and θ_{pitch} = 10°.

The results in Fig.18 show that, when the airfoil camber increases:

- The rotational speed steadily decreases ($\sim -800RPM$), meaning that more cambered airfoils generate more thrust at the same rotational speed;
- 1st BPF total SPL and both loading and thickness noise components decrease monotonically;
- The power loading exhibits a peak for 1% maximum camber and then it decreases.

As the results of Fig.18 show, from the aerodynamic point of view, adding 1% camber to the 12% thick NACA airfoil improves the aerodynamic efficiency and, as a consequence, increases the flight time. Winslow et al. [35] studied the influence of the maximum camber on NACA X403 airfoils and pointed out that, at low Reynolds numbers (2×10^4 and 1×10^5), the more cambered airfoils got higher lift peaks, higher drag and, overall, higher efficiency. They concluded that, at these Reynolds numbers, 4% cambered airfoils are the ones to choose when efficiency is the main objective. Here, higher cambered airfoils led to rotor rotating at lower speeds, which means that the more the airfoil is cambered, the higher is the lift created by the airfoil and the larger the rotor thrust at the same rotational speed. However, the most efficient airfoil in this study is the one with 1% camber. XFOIL simulations on rotors section at 87% of the blade span showed that, by increasing the maximum camber from 0% to 1%, the LSB and the turbulent transition are pushed towards the trailing edge. It increases the low pressure region on the suction side that leads to overall higher lift coefficient. This, coupled to the unchanged drag coefficient, conducts to higher lift-to-drag ratio and more efficient rotors. The LSB are bigger for maximum cambers above 2%, and the trailing edge separation occurs at high cambers. This is the main reason why both lift and drag coefficients are increased, but the overall efficiency is not. While the NACA 1512 is the most efficient airfoil from the aerodynamic point of view, it is not from the aeroacoustic one. Since higher cambered airfoils produce more lift, the rotational speed needed to reach 2N thrust is lower and, as a direct consequence, 1st BPF SPL of total, loading and thickness noise components are reduced. In this case, even if the airfoil thickness distribution is unchanged, the thickness noise decreases. In light of the results presented in this subsection, MAV propellers working at low Reynolds number conditions are more efficient with cambered airfoils. For thick airfoils like the NACA x512 series, the ideal camber is 1%. Above that value, the drag coefficient increases at a higher rate than the lift coefficient, leading to less efficient rotors. Attention must be paid when choosing the camber of the airfoil. In fact, this design input is linked to the Reynolds number at which the rotor will operate, but also on the airfoil thickness.

V. Conclusion

The aerodynamic performance and the aeroacoustic footprint of quadcopter rotors are highly dependent on the rotor geometry and their operating Reynolds number. The low Reynolds number typical of micro air vehicles (MAVs) leads to new design challenges that the research community has tried to overcome these last decades by developing new low-order fidelity simulation codes and optimization methodologies.

Here, a non-linear vortex lattice/particle method (NVLM/VPM) code coupled with the Farassat formulation-1A of the Ffowcs-Williams & Hawkings (FW-H) acoustic analogy is validated upon results from the literature and experimental results on a NACA0012 constant pitch rotor. The NVLM code is then used to analyze the directivity of the 1st blade passing frequency (BPF) sound pressure level (SPL). The influence of the blade pitch angle and the airfoil shape on the aerodynamic performance and the tonal noise emitted by the rotor is also studied.

Preliminary results presented in this paper showed the tonal noise directivity shape of the 1st and 2nd BPF. The 1st one was studied more in details and destructive/constructive interferences phenomena between the thickness and the steady loading noise are demonstrated. The steady loading noise is also shown to be more important than the unsteady loading noise and its directivity is equivalent to the directivity of a rotating dipole with same rotational speed, total thrust and torque as the full rotor. In order to reproduce the same directivity, the dipoles should be positioned at a radius equal to 80% of the blade radius. Another constructive/destructive interferences are shown to be the causes of the non-symmetrical shape of the steady loading noise.

The influence of the pitch of the blades is then studied. It affects the sectional lift coefficient, hence the rotational speed needed to withstand the 2N thrust decreases as well as the tonal noise. The power loading reaches a maximum value at 14° pitch angle and decreases beyond this value.

Then, different airfoil thicknesses going from 7% to 12% are studied, with a constant pitch angle of 10°. For an isothrust of 2N, the best configuration is the one with 8% maximum thickness. Increasing this value affects the airfoil performance and, as a consequence, the rotor one. The overall lift coefficient increases with the thickness, resulting in lower rotational speed to reach 2N. However, the torque increases as well and, above 8% thickness, it increases more

than the thrust, leading to lower power loading. As expected, the thickness noise increases with the airfoil thickness while the loading noise does not and becomes even lower than the thickness noise at 11% thickness. This means that, decreasing the thickness has more benefits than drawbacks. But thinner airfoils lead also to lighter and less stiff blades. Last, a camber can be added to the airfoil in order to increase the efficiency of the airfoil and, overall, of the whole rotor. A more pronounced camber pushes the laminar separation bubble towards the trailing edge. This increases the low pressure region on the suction side and leads to higher lift coefficients and more efficient airfoils up to a certain limit. In fact, while for thin airfoils (3% thick) the camber that gives the most efficient rotor is 4%, in the present investigated case of 12% thick airfoils the most efficient airfoil has a camber of 1%. Highly cambered airfoils produce more thrust, thus the rotational speed to reach 2N thrust is decreased. This reduction in the speed leads to lower SPL. Cambered airfoils should be chosen to obtain aerodynamic and aeroacoustic improvements.

In the rotor design phase, different parameters need to be taken into account and can help in reaching the objective performance. The pitch angle and the airfoils are two important parameters. Increasing the first one can easily lead to more efficient and less noisy rotors at the same time. The second one is more complex: the aerodynamic performance of the airfoil can be improved by playing on both thickness and camber distribution. However these parameters are non-linearly dependent on the Reynolds number. This means that there is not an airfoil that optimize the aerodynamic performance over a wide range of Reynolds number. In the 25cm diameter constant pitch rotor studied in this paper, thinner cambered airfoils are the best one for both aerodynamic and aeroacoustic performance. The study presented here takes into account only tonal noise in the aeroacoustic analysis. Even if the tonal part of the acoustic spectrum has the highest peaks, the broadband noise contains much more frequencies that disturb the human ear. In the future, the full acoustic spectrum will be approximated by adding semi-empirical methods to the present NVLM/VPM code.

Acknowledgments

This work has been financed by Parrot Drones SAS and the Association Nationale Recherche Technologie (ANRT), realized at ISAE-SUPAERO and performed using HPC resources from PANDO (ISAE-SUPAERO), GENCI [CCRT-CINES-IDRIS] (Grant 2021-[A0102A07178] and 2022-[A0122A07178].

References

[1] Lee, H., and Lee, D. J., "Rotor interactional effects on aerodynamic and noise characteristics of a small multirotor unmanned aerial vehicle," *Physics of Fluids*, Vol. 32, No. 4, 2020. https://doi.org/10.1063/5.0003992, URL https://doi.org/10.1063/5.0003992.

[2] Alvarez, E. J., Schenk, A., Critchfield, T., and Ning, A., "Rotor-on-Rotor Aeroacoustic Interactions of Multirotor in Hover," *Journal of the American Helicopter Society*, 2020. URL https://github.com/byuflowlab/FLOWUnsteady.

[3] Zawodny, N. S., and Boyd, D. D., "Investigation of rotor-airframe interaction noise associated with small-scale rotary-wing unmanned aircraft systems," *Annual Forum Proceedings - AHS International*, 2017, pp. 66–82. https://doi.org/10.4050/jahs.65.012007.

[4] Ariza, D. G., ""Study of the sensitivity to the lateral wind of a Mini Unmanned Aerial Vehicle with VTOL flight capabilities"," *Institut Supérieur de l'Aéronautique et de l'Espace (ISAE)*, 2013.

[5] Serré, R., Gourdain, N., Jardin, T., Delattre, G., and Moschetta, J. M., "Analysis of the flow produced by a low-Reynolds rotor optimized for low noise applications. Part II: Acoustics," *43rd European Rotorcraft Forum, ERF 2017*, Vol. 2, 2017, pp. 799–805.

[6] Serré, R., Gourdain, N., Jardin, T., Jacob, M. C., and Moschetta, J. M., "Towards silent micro-air vehicles: optimization of a low Reynolds number rotor in hover," *International Journal of Aeroacoustics*, Vol. 18, No. 8, 2019, pp. 690–710. https://doi.org/10.1177/1475472X19890260.

[7] Nana, C., Yann, M., and Serré, R., "Fast Multidisciplinary Optimization of a MAV propeller for noise reduction: from simulation to experimentation," *53rd 3AF International Conference on Applied Aerodynamics*, , No. June, 2018.

[8] Wisniewski, C. F., Byerley, A. R., Heiser, W. H., Van Treuren, K. W., and Liller, W. R., "Designing small propellers for optimum efficiency and low noise footprint," *33rd AIAA Applied Aerodynamics Conference*, , No. June, 2015, pp. 1–17. https://doi.org/10.2514/6.2015-2267.

[9] Boyer, F., and Drapier, A., "Multidisciplinary optimization of a MAV propeller for noise reduction," 2017, pp. 301–306.

[10] Wilke, G., "Findings in Aero-Acoustic Simulations for Optimizations," *76th Annual Forum*, Virtual, 2020. URL https://elib.dlr.de/136612/.

[11] Li-Volsi, P., Gomez-Ariza, D., Jardin, T., Gojon, R., and Moschetta, J.-M., "Design of aeroacoustically stealth MAV rotors," *12^{th} International Micro Air Vehicle Conference*, edited by J. Martinez-Carranza, Puebla, México, 2021, pp. 153–160. URL http://www.imavs.org/papers/2021/19.pdf, paper no. IMAV2021-19.

[12] Li-Volsi, P., Gomez-Ariza, D., Gojon, R., Jardin, T., and Moschetta, J.-M., "Aeroacoustic optimization of MAV rotors," *International Journal of Micro Air Vehicles*, Vol. 14, 2022, pp. 1–11. https://doi.org/10.1177/17568293211070827.

[13] Gojon, R., Jardin, T., and Parisot-Dupuis, H., "Experimental investigation of low Reynolds number rotor noise," *The Journal of the Acoustical Society of America*, Vol. 149, No. 6, 2021, pp. 3813–3829. https://doi.org/10.1121/10.0005068, URL https://doi.org/10.1121/10.0005068.

[14] Gojon, R., "JASA_2021_GOJON_JARDIN_PARISOT-DUPUIS," , 2021. https://doi.org/10.34849/C73YB7, URL https://doi.org/10.34849/C73YB7.

[15] Katz, J., and Plotkin, A., *Low-Speed Aerodynamics*, Cambridge University Press, New York, NY, USA, 2012, p. 10013–12473.

[16] Jo, Y., Lee, H., and Lee, D. J., "Prediction of rotor flow for unmanned aerial system using nonlinear vortex lattice method," *6th Asian-Australian Rotorcraft Forum and Heli Japan 2017, ARF 2017*, 2017.

[17] Drela, M., "XFOIL: An Analysis and Design System for Low Reynolds Number Airfoils," *Low Reynolds Number Aerodynamics*, edited by T. J. Mueller, Springer Berlin Heidelberg, Berlin, Heidelberg, 1989, pp. 1–12.

[18] Mack, L. M., "Transition and laminar instability," 1977.

[19] Jo, Y., Jardin, T., Gojon, R., Jacob, M. C., and Moschetta, J.-M., *Prediction of Noise from Low Reynolds Number Rotors with Different Number of Blades using a Non-Linear Vortex Lattice Method*, 2019. https://doi.org/10.2514/6.2019-2615, URL https://arc.aiaa.org/doi/abs/10.2514/6.2019-2615.

[20] Hubbard, H., "Aeroacoustics of Flight Vehicles: Theory and Practice Volume 1: Noise Sources," *NASA Reference Publication*, Vol. 1, No. 1258, 1991, p. 610. URL http://www.dtic.mil/dtic/tr/fulltext/u2/a241141.pdf#page=16.

[21] Burley, C. L., and Brooks, T. F., "Rotor Broadband Noise Prediction with Comparison to Model Data," *Journal of the American Helicopter Society*, Vol. 49, No. 1, 2004, pp. 28–42. https://doi.org/10.4050/jahs.49.28.

[22] Farassat, F., and Succi, G. P., ""The Prediction of Helicopter Discrete Frequency Noise"," *Vertica*, Vol. 7, No. 4, 1983, p. 309–320.

[23] Deters, R. W., Ananda, G. K., and Selig, M. S., "Reynolds number effects on the performance of ailerons and spoilers," *39th Aerospace Sciences Meeting and Exhibit*, , No. June, 2001, pp. 1–43. https://doi.org/10.2514/6.2001-908.

[24] Casalino, D., "An advanced time approach for acoustic analogy predictions," *Journal of Sound and Vibration*, Vol. 261, No. 4, 2003, pp. 583–612. https://doi.org/10.1016/S0022-460X(02)00986-0.

[25] Rienstra, S., and Hirschberg, A., *An introduction to acoustics*, IWDE report, Technische Universiteit Eindhoven, 2001.

[26] Hirsch, C., Ghorbaniasl, G., and Ramboer, J., "Fan Noise Simulation in the Time Domain : Validation Test Cases," , No. January, 2003.

[27] Ghorbaniasl, G., and Hirsch, C., "Validation and application of a far-field time domain formulation for fan noise prediction," *Collection of Technical Papers - 11th AIAA/CEAS Aeroacoustics Conference*, Vol. 1, No. May, 2005, pp. 497–511. https://doi.org/10.2514/6.2005-2838.

[28] Brentner, K. S., "Prediction of Helicopter Rotor Discrete Frequency Noise," 1986.

[29] Parisot-Dupuis, H., Gojon, R., Jardin, T., Jo, Y., Doué, N., and Moschetta, J.-M., "Experiments on UAV rotor noise at low Reynolds and low Mach numbers," *Quiet Drones*, October 2020.

[30] Jardin, T., Prothin, S., and Magana, C. G., "Aerodynamic performance of a hovering microrotor in confined environment," *Journal of the American Helicopter Society*, Vol. 62, No. 2, 2017, pp. 1–7. https://doi.org/10.4050/JAHS.62.022008.

[31] Jacobs, J., Ward, K., and Careas, R., "The Characteristics of 78 Related Airfoil Sections Sections From Tests In The Variable-Density Wind Tunnel," *National Advisory Commitee for Aeronautics*, 1935.

[32] Leishman, G. J., *Principles of helicopter aerodynamics / J. Gordon Leishman,...*, second edition ed., Cambridge aerospace series, Cambridge University Press, New York, right 2006.

[33] De Paula, A. A., Kleine, V. G., and Porto, F. D. M., "The thickness effects on symmetrical airfoil flow characteristics at low Reynolds number," *AIAA SciTech Forum - 55th AIAA Aerospace Sciences Meeting*, , No. January, 2017. https://doi.org/10.2514/6.2017-1422.

[34] Jacobs, E., and Sherman, A., "Airfoil section characteristics as affected by variations of the Reynolds number," 1939.

[35] Winslow, J., Otsuka, H., Govindarajan, B., and Chopra, I., "Basic understanding of airfoil characteristics at low Reynolds numbers (104–105)," *Journal of Aircraft*, Vol. 55, No. 3, 2018, pp. 1050–1061. https://doi.org/10.2514/1.C034415.